

Response of Early Winter Haze in the North China Plain to Autumn Beaufort Sea Ice

Zhicong Yin^{1,2}, Yuyan Li¹, Huijun Wang^{1,2}

¹Key Laboratory of Meteorological Disaster, Ministry of Education / Joint International Research Laboratory of Climate and Environment Change (ILCEC) / Collaborative Innovation Center on Forecast and Evaluation of Meteorological Disasters (CIC-FEMD), Nanjing University of Information Science & Technology, Nanjing 210044, China

²Nansen-Zhu International Research Centre, Institute of Atmospheric Physics, Chinese Academy of Sciences, Beijing, China

Correspondence to: Yuyan Li (yyan370@163.com)

Abstract. Recently, early winter haze pollution in the North China Plain has been serious and disastrous, dramatically damaging human health and the social economy. In this study, we emphasized the close connection between the number of haze days in early winter in the North China Plain and the September-October sea ice in the west of the Beaufort Sea ($R=0.51$) via both the observational analyses and numerical experiments. Due to efficient radiative cooling, the responses of atmospheric circulations partially manifested as reductions of surface wind speed over the Beaufort Sea and Gulf of Alaska, resulting in a warmer sea surface in the subsequent November. The sea surface temperature anomalies over the Bering Sea and Gulf of Alaska acted as a bridge. The warmer sea surface efficiently heated the above air and led to suitable atmospheric backgrounds to enhance the potential of haze weather (e.g., a weaker East Asia jet stream and a Rossby wave-like train propagated from North China and the Japan Sea, through the Bering Sea and Gulf of Alaska, to the Cordillera Mountains). Near the surface, the weakening sea level pressure gradient stimulated anomalous southerlies over the coastal area of China and brought about a calm and moist environment for haze formation. The thermal inversion was also enhanced to restrict the underswing of clear and dry upper air. Thus, the horizontal and vertical dispersion were both limited, and the fine particles were apt to accumulate and cause haze pollution.

Keywords: Haze, Pollution, Aerosol, Sea ice, Arctic, Climate change

1. Introduction

During the past few years, the increase of surface air temperature has been distinctly amplified in the Arctic region and approximately twice as large as the average increase in global warming, which was called the Arctic Amplification (Zhou, 2017). Arctic sea ice (ASI) decreases rapidly since the satellite era, in particular, after the year of 2000 (Gao et al., 2015). The change of ASI, associated with changed reflection of solar radiation and exchange of energy and fresh water, could remotely connect with the climate in the Northern Hemisphere, especially the winter climate in Eurasia (Liu et al., 2007; Wang and Liu, 2016). The decreased ASI over the Barents–Kara Seas in late autumn stimulated a planetary-scale Rossby

30 wave train in early winter (Honda et al., 2009; Kim et al., 2014) and transported its impacts to Eurasia. The variation of the
autumn ASI had significant impacts on the East Asian jet stream and the East Asian trough (Li and Wang, 2013) as well as
the winter Arctic Oscillation (Li and Wang, 2012; Li et al., 2015) and the East Asian winter monsoon (Li and Wang, 2014; Li
et al., 2014). Since 2000, the snowfall in Siberia has been enhanced, which is probably related to the increased moisture flux
35 resulted in more blocking patterns and water vapor, which was a benefit for heavy snowfall in Europe during early winter
and in the United States during winter. Furthermore, under the positive Pacific decadal oscillation phase, the autumn ASI
reduction contributed to the subseasonal variability of surface air temperature in the East Asian winter (Xu et al., 2018; He,
2015). The dust (dry particles suspended in air after strong wind) and sandstorm (strong wind carrying sands) over North
China, types of weather that are sensitive to wind, also showed close relationships with the variation of ASI after the
40 mid-1990s (Fan et al., 2017). The sea ice over the Barents–Kara Seas induced dust-related atmospheric circulations (e.g., a
strengthened East Asian jet, increased cyclogenesis, and greater atmospheric thermal instability).

Haze (polluted particulate aerosols suspended in air), also being sensitive to wind, frequently occurred under calm and
static weather conditions, i.e., small surface winds and strong thermal inversion (Yin et al., 2015; Ding and Liu, 2014; Chen
and Wang, 2015; Cai et al., 2017; Gao and Chen, 2017). For the long-term trend of number of haze days, human activities
45 are the recognized and fundamental driver (Li et al., 2018; Yang et al., 2016; Chen et al., 2018; Zhang et al., 2018), but the
rapid ASI decline also contributed to the trend of number of haze days in the North China Plain after 2000 (Wang and Chen
2016). For the interannual to interdecadal variations, the impacts of ASI on the number of haze days in the east of China
were emphasized by observational analyses (Wang et al., 2015) and numerical studies (Li et al., 2017). By the sensitive
experiments, Li et al. (2017) emphasized the impacts of ASI anomalies on haze pollution in North China, but deemphasized
50 the role of ENSO (He et al., 2019). From 1979–2012, the ASI loss led to a northward shift of the East Asia jet stream and
weak East Asian winter monsoons, indicating a strongly negative correlation with the number of haze days in the east of
China (Wang et al., 2015). However, the first mode of the Empirical Orthogonal Function (EOF) in Yin and Wang (2016a)
presented different variations of number of haze days in the south and north of the Yangtze River. The positive relationship
between the autumn sea ice in the Beaufort Sea and the number of haze days in winter was briefly revealed without sufficient
55 physical explanations but contributed to the prediction of number of haze days in winter (Yin and Wang, 2016b, 2017b). The
number of haze days in early winter (December–January) also varied differently with that in February (figure omitted),
suggesting a potential different driving mechanism. Thus, an open question still existed, i.e., the connections between
Beaufort Sea ice (BSI) and the number of haze days in early winter in the North China Plain (NCP: 34–42°N, 114°E–120°E)
and the associated physical mechanisms.

60 2. Datasets and methods

The monthly sea ice concentrations ($1^\circ \times 1^\circ$) were downloaded from the Met Office Hadley Center (Rayner et al., 2003), which is widely used in the sea ice-related analysis. The number of haze days were mainly calculated with the 6-hr observed visibility and relative humidity. The observed relative humidity, visibility, wind speed, and weather phenomena data used here were collected and controlled by the National Meteorological Information Center, China Meteorological Administration.

65 The computing method of haze days was in accordance with Yin et al. (2017). That is, if the visibility was lower than 10km and the relative humidity was drier than 90%, the day was defined as one haze day after filtering the other weather affected visibility (i.e., precipitation, dust, sandstorm, etc.). The hourly $PM_{2.5}$ concentration data were provided by the Ministry of Environmental Protection of China, including 162 sites in the North China. The daily maximum $PM_{2.5}$ was the maximum value obtained over 24-hour measurements. The $1^\circ \times 1^\circ$ ERA-Interim data used here included the geopotential height (Z),

70 zonal and meridional wind, specific humidity, vertical velocity, air temperature at different pressure levels, sea level pressure (SLP), boundary layer height and surface air temperature data (Dee et al., 2011). The monthly mean sea surface temperature (SST) datasets, with a horizontal resolution of $1^\circ \times 1^\circ$, were also derived from the website of ERA-Interim (Dee et al., 2011). The $2.5^\circ \times 2.5^\circ$ monthly reanalysis heat fluxes (i.e., the sensible heat net flux and the latent heat net flux) were available on the website of the National Center for Environmental Prediction and the National Center for Atmospheric Research (Kalnay et al., 1996). The simulations from the Community Earth System Model Large Ensemble (CESM-LE) datasets are employed

75 (Kay et al., 2015). There are 35 member ensembles in the CESM-LE simulations that completed at NCAR, with a horizontal resolution of 0.9° latitude \times 1.25° longitude and 30 vertical levels. The CESM-LE simulations were completed by the fully coupled CESM model.

3. Variation of the early winter haze

80 In most of the observational sites in the east of China, the number of haze days in December and January (HDJ) accounted for more than 70% of the total number of haze days in winter (Figure 1), indicating that the haze pollution in the early winter was more serious than that in February. Yin et al. (2018) also illustrated that the inter-annual variation of number of haze days in February was different from that in the early winter. Thus, it is necessary to analyze the features of haze pollution in the early winter and associated climate drivers. The observational HDJ were decomposed by the EOF method

85 and the variation contribution of the first and second modes were 33% and 14%, respectively. In the first mode, the HDJ in the south and north of the Yangtze River varied differently (Figure 1) and should have a distinguishing relationship with the autumn ASI. In this study, we focused on the HDJ in the NCP region (HDJ_{NCP} , i.e., mean of the 38 sited HDJ) and its connection with the autumn ASI.

The HDJ_{NCP} was stable during 1979 to 1992 and decreased from 1993 to 2009. After 2009, the HDJ_{NCP} showed a strong upward trend. The minimum HDJ_{NCP} occurred in 2010, which was 17.5 days. Afterwards, the HDJ_{NCP} increased dramatically and persistently, reaching a maximum (i.e., 42.7 days) in 2015. The mass concentration of PM_{2.5} is an important indicator of haze pollution. The daily maximum of area-mean PM_{2.5} in 2015 is shown in Figure 2b and was above 100 μg/m³. The concentrations of PM_{2.5} were relatively lower in January 2016 than those in December but still exceeded the threshold of pollution in China (i.e., 75 μg/m³). On 23 December, the most disastrous haze occurred, and the area-mean PM_{2.5} concentration approached 500 μg/m³, indicating quite poor air quality and a serious health risk.

4. Connection with ASI and associated physical mechanisms

As illustrated by Wang et al. (2015), the autumn ASI significantly and negatively affected the haze pollution in the east of China by modulating the large-scale atmospheric circulations and local meteorological conditions. Furthermore, the opposite pattern of number of haze days in the east of China was revealed in Figure 1. To confirm the response of HDJ_{NCP} to the autumn sea ice, the correlation coefficients between the HDJ_{NCP} and the September-October sea ice were assessed after removing the linear trend (Figure 3). A positive correlation was found from the East Siberian Sea to the Beaufort Sea. In this broad region, the significantly correlated area was intensively located over the west of the Beaufort Sea. Thus, the area-averaged September-October sea ice area over the west of the Beaufort Sea (73–80 °N, 146 °W–178 °W) was calculated and denoted as the BSISO index, whose correlation coefficient with HDJ_{NCP} was 0.51 (above the 99% confidence level) after removing the linear trend. This apparent positive relationship indicates that the efficient accumulation of the preceding autumn sea ice over the west of the Beaufort Sea significantly intensified the number of haze days in early winter over the NCP area. To confirm this connection, the year-to-year change of the sea ice concentration was examined (Figure 4). From 1979 to 2015, there were seven years with significantly negative BSISO (i.e., BSISO < -0.8 × its standard deviation), and ten years with significantly positive BSISO (i.e., BSISO > 0.8 × its standard deviation). During 65% of these years, the significant BSISO anomalies corresponded HDJ_{NCP} anomalies with the same mathematical sign. There were no significantly opposite responses of HDJ_{NCP} (|HDJ_{NCP} | > 0.8 × its standard deviation) to the BSISO anomalies. Furthermore, the relationship seemed to be enhanced after the mid-1990s. The same mathematical signs of the anomalies appeared more frequently.

The positive sea ice anomalies, with high albedo, can efficiently reflect solar radiation and restore more fresh water, which could influence the local and adjacent SST. The correlation coefficients between BSISO and the simultaneous and subsequent SST were computed (Figure 5). Because of efficient reflections of the solar radiation, the locally negative SST anomalies, located near the west of the Beaufort Sea (70–81 °N, 166 °E–138 °W), were associated with the positive BSISO anomalies in October. In the following two months, these negative SST anomalies could not be sustained, i.e., these anomalous responses disappeared in November. However, the positive SST anomalies in the Bering Sea (49–60 °N,

165 °W–180 °W) and the Gulf of Alaska (40–52 °N, 130 °W–165 °W) appeared in October and were persistently enhanced in
120 November and December. These three significantly correlated SSTs, located near the west of the Beaufort Sea (WB), over
the Bering Sea (BS) and the Gulf of Alaska (GA), were defined as SST_{WB} , SST_{BS} and SST_{GA} , respectively. The correlation
coefficients between these three indices were enumerated in Table 1 to present the change of the relationship with SST.
Over time, the linkage between BSISO and local SST (i.e., SST_{WB}) rapidly receded. To confirm the role of the local SST on
the HDJ_{NCP} , the correlation coefficient between HDJ_{NCP} and SST_{WB} was -0.30 in October (exceeding the 95% confidence
125 level), and -0.05 and -0.10 in the following November and December (insignificant). However, the correlation coefficients
between the SST_{BS} (SST_{GA}) and BSISO were persistent and even became enhanced in November and December (Table 1).
We speculated that the November SST_{BS} and SST_{GA} was the junction between the BSISO and HDJ_{NCP} .

According to the numerical results illustrated by Deser and Tomas (2007), the responses of atmospheric circulations to
sea ice anomalies were initially baroclinic in the first 5–10 days and progressively became more barotropic and increased in
130 both spatial extent and magnitude within 2 months. In September and October, due to the radiative cooling of the positive
BSISO anomalies, the baroclinic responses of the atmospheric circulations manifested mainly as anomalous cyclonic
circulation in the upper troposphere (Figure 6a). There were also weak anti-cyclonic responses in the Bering Sea and Gulf of
Alaska. In the subsequent November, the extent of these cyclonic and anti-cyclonic anomalies increased, especially the
anti-cyclonic circulations over the Bering Sea and Gulf of Alaska (Figure 6b). The barotropic structure of the atmospheric
135 responses became more obvious, i.e., there were also cyclonic and anti-cyclonic circulations on both sides of the Beaufort
Sea, near the surface (Figure 6d). In addition, there were also positive SLP anomalies near the Aleutian Islands, indicating a
weak Aleutian Low. Near the surface, a significant anomalous southerly was existed between cyclonic and anti-cyclonic
circulations, and an anomalous east wind was excited in the south of the anti-cyclonic circulation (Figure 6d). Overlapping
with the climate mean state, the surface wind speeds over the RS1 (41–54 °N, 140 °W–165 °W) and RS2
140 (70–76 °N, 140 °W–170 °W) regions were significantly receded (Figure 7). The area-average surface wind speed was then
calculated and denoted as $WSPD_{RS1}$ and $WSPD_{RS2}$ to examine its impacts on the simultaneous SST. In November, the
climatological northeasterly through the Bering Strait transported cold seawater from the Arctic to the Bering Sea and
resulted in a lower SST. The correlation coefficient between $WSPD_{RS2}$ and SST is shown in Figure 8 and was significantly
negative in the Bering Sea. The driver of the cold seawater transportations, i.e., the surface wind, decreased and led to
145 warmer SST_{BS} in November. Another reduction of surface wind speed, i.e., $WSPD_{RS1}$, indicated the weakening of the west
surface wind and accompanying subdued evaporation near the sea surface. This RS1 region was located consistently with the
warmer Gulf of Alaska. The correlation coefficients between the $WSPD_{RS1}$ and SST_{GA} were significantly negative, indicating
that the reduction of $WSPD_{RS1}$ resulted in a warmer sea surface over the Gulf of Alaska (Figure 9a). Due to the weakening of
the water evaporation, the latent heat release slowed down both in the Bering Sea and the Gulf of Alaska, which conserved

150 more thermal energy in the sea surface (Figure 9b). In addition, the upper anti-cyclonic circulations, with clear sky, facilitated more shortwave solar radiation onto the sea surface. The absorbed and stored thermal energy, which was connected with the positive BSISO anomalies, heated the sea surface over the Gulf of Alaska in November, i.e., positive SST_{GA} anomalies. Both of the SST_{GA} and SST_{BS} were significantly influenced by the BSISO and synchronously changed (figure omitted). Thus, the SST_{BS} and SST_{GA} were integrated as SST_{BA} to analyze their corporate impacts on the HDJ_{NCP}.
155 The variations of November SST_{BA} and the BSISO were strongly consistent, especially after 2000 (Figure 10). As presented in Table 1, from October, the SST_{BA} began to significantly connect with the BSISO. Over time, this connection persisted and strengthened. The correlation coefficient between November (December) SST_{BA} and the BSISO was 0.43 (0.48), exceeding the 99% significance test.

Statistically, the November SST_{BA} was significantly correlated with the HDJ_{NCP} (i.e., the correlation coefficient was
160 0.61 and above the 99% confidence level), showing strong impacts on the number of haze days in early winter over the NCP region. To reveal the physical processes, the associated atmospheric circulations and local meteorological conditions were diagnosed in Figures 11–15. The warmer sea surface efficiently heated the above air and resulted in ascending motion from the Gulf of Alaska to the Aleutian Islands, which could extend to the atmosphere at 200 hPa (Figure 11). Furthermore, significant accompanying descending motions at 200 hPa were stimulated from the Sea of Okhotsk to the Hawaiian Islands
165 (Figure 11a). Near the surface, there was also a sinking motion over the Hawaiian Islands (Figure 11b). On the mid-troposphere, the significantly negative Z500 anomalies, i.e., cyclonic circulations, were exerted above the warmer Bering Sea and Gulf of Alaska (Figure 12b). The responses of the December-January atmospheric circulations to the warmer November SST_{BA} showed deeply barotropic structures. There were also significant cyclonic circulations in the lower troposphere (Figure 12c) and near the surface (Figure 12d). At 500 hPa, there were significant anti-cyclonic anomalies
170 located on both sides of the cyclonic circulations, i.e., over North China, the Japan Sea, and the Cordillera Mts. Thus, a Rossby wave-like train was induced by the SST_{BA}, which propagated from North China and the Japan Sea, through the Bering Sea and Gulf of Alaska, to the Cordillera Mts. This “+—+” pattern could also be recognized in the lower (Figure 12c) and upper (Figure 12a) troposphere. The anti-cyclonic circulations over North China and the Japan Sea were recognized as the key atmospheric system to influence the haze pollution in the NCP area (Yin and Wang, 2016a; Yin et al., 2017). To
175 confirm the linkage between this Rossby wave-like train and SST_{BA}, the area-averaged Z500 in three centers ([88 °E–115 °E, 30–50 °N], [150 °E–160 °W, 45–60 °N], [115 °W–130 °W, 50–60 °N]) were calculated and are shown in Figure 13. The correlation coefficients between the three centers, from west to east, with SST_{BA} were 0.47, –0.46, and 0.37, all above the 95% confidence level. Due to the change of the pressure gradient, there were positive zonal westerlies from Lake Baikal to the Hawaiian Islands and negative westerly anomalies from East China to the west subtropical Pacific (Figure 12a). Therefore,
180 zonal west winds prevailed in the mid-high latitude, and the meridionality of the atmosphere was reduced. The East Asia jet

stream was weakened by anomalous easterlies and shifted northwards, indicating the decrease of the southward cold air activities. In addition, the southern section of the East Asia major trough, which reached the NCP area and guided cold air southward, was truncated by the anomalous anti-cyclonic circulations (Figure 12b). In contrast, due to the cyclonic anomalies over the Aleutian area, the northern section of the East Asia major trough was enhanced but moved eastward. 185 These large-scale anomalous atmospheric circulations could provide a suitable background for the enhancement of the potential of the haze weather (Yin and Wang, 2017a).

Near the surface, because of the SST_{BA} heating, the Aleutian Low moved eastward and was enhanced over the Bering Sea and Gulf of Alaska. Consistent with the barotropic anomalies in the above air, there were positive SLP anomalies from Northeast China to the west Pacific (Figure 12d). That is, a north-south seesaw over the North Pacific was discerned clearly, 190 similar to the anomalous North Pacific Oscillation (NPO) pattern (Rogers, 1981). The difference of SLP ($[140^{\circ}E-170^{\circ}W, 20-30^{\circ}N]$ minus $[165^{\circ}E-155^{\circ}W, 48-65^{\circ}N]$) was calculated to quantify this seesaw pattern, whose correlation coefficients with the BSISO, SST_{BA} and HDJ_{NCP} were 0.33, 0.64 and 0.61, respectively. Bounded by the east of China, the south positive center of NPO and the negative anomalies occupied the west Pacific and Eurasia, respectively. The drivers of the East Asian winter monsoon, i.e., the pressure gradient between the continent and the ocean, became weak, indicating the limitation of 195 cold air and ventilation conditions. Compared to the local zonal wind, the meridional wind played more important roles on weakening the horizontal dissipation conditions of the air (Figure omitted). The southerly anomalies were located over the coastal area of China and transported moisture to the NCP area (Figure 14a), providing moist air for haze formation. In winter, the anomalous south winds also weakened the prevailing northerly and reduced the invasion of cold air. The humid atmosphere was conducive to the hygroscopic growth of pollutant particles, which reduced the visibility rapidly and 200 structured stable weather conditions. The surface wind speed, indicating the horizontal dispersion capacity of the atmosphere, also subsided. In addition, the shallow thermal inversion layer or the boundary layer limited the upward dispersion of the pollutant particles. As shown in Figure 14b, the intensity of the thermal inversion over the NCP area was significantly heightened, while the boundary layer significantly declined. Generally, the air on the high altitude was relatively dry and clean. The sinking of the upper air to the surface was an important approach in dispersing the surface pollution (Sun et al., 205 2017). Instead, the upward motion above the boundary layer resisted the breaking of the thermal layer and was in favor of haze occurrence (Figure 15a). The associated anomalous descending flow was blocked in the north of $46^{\circ}N$, which was consistent with the location of the northward cold air activities (Figure 15a). Influenced by the warmer SST_{BA} , there were anomalous ascending motions over the NCP area. Thus, the weakened downward transportation of momentum was not sufficient to enhance the winds near the surface and break the thermal inversion layer. Therefore, the clear, dry and cold air 210 was difficult to transport to the surface, indicating the failure of the blowing wind. Under poor ventilation conditions, i.e., the horizontal and vertical dispersion was limited, the fine particles were apt to accumulate and cause haze pollution. Combined

with favorable moisture conditions, the haze exacerbated rapidly and perniciously.

5. Causality verification by CESM-LE experiments

The connection between the haze pollution in North China and ASI, and associated physical mechanisms were statistically analyzed in the above sections. To confirm the causality, numerical experiments were designed with the public CESM-LE datasets. To be consistent with the observational results, the variables from CESM-LE from 1979 to 2015 are employed, which was combined by the historical simulation during 1979–2005 and the data during 2006–2015 from the future representative concentration pathway 8.5 forcing simulation. 35 CESM-LE ensemble members were used here. The CESM-LE simulations were completed by the fully coupled CESM model, thus the interactions among sea ice, sea temperature and atmosphere can be contained. The years when the sea ice anomalies concentrated in the west of the Beaufort Sea were selected and the differences between the positive BSISO and negative BSISO years were identified as the responses to the sea ice anomalies. In the numerical experiment, all available CESM-LE members were included and different amplitudes of sea ice anomalies were composited, thus the uncertainty from the internal variability were largely reduced.

In Figure 16a, the sea ice anomalies were obvious in the key region. The maximum of the difference in sea ice concentration was more than 35% (Figure 16a). In the following November, the accumulated sea ice favored increased SST over the Gulf of Alaska (Figure 16b), which is in good accordance with the observed results. Although there were weaker, but negative SST responses in Bering Sea, the positive SST anomalies extended southwards and enhanced the air-sea interaction. In terms of the corresponding atmospheric circulations with regard to anomalous BSISO, the composite difference was also consistent with the observed results. The anti-cyclonic anomalies of the geopotential height at 500hPa were also well reproduced by the numerical model in the early winter (Figure 16c). On the lower troposphere, there were also anomalous anticyclone over North China and Northeast China, which induced anomalous southerlies (Figure 16d) and weakened the cold air from the high latitude. Furthermore, the moist air condition (Figure 16c) and lower boundary layer (Figure 16d) were also verified to be significantly connected with the positive BSISO anomalies. Consistent with the observed results, the linkages between the BSISO and the haze pollution in the North China also exist in CESM-LE simulations. Meanwhile, the corresponding physical mechanisms were also well reproduced by the large ensemble members. The performances of numerical models in the mid-high latitude were consistently limited, however, the results from CESM-LE here successfully captured major features and general physical processes as expected. Consequently, the robustness of the proposed connections and physical mechanisms were strongly confirmed.

In the sub-seasonal scale, the haze weather in early winter occurred more frequently and varied differently from that in February. In this study, the close relationship between number of haze days in early winter in the NCP area and the September-October sea ice in the west of the Beaufort Sea, with correlation coefficient = 0.51, was revealed. The positive September-October sea ice anomalies over the west of the Beaufort Sea strongly intensified the early winter haze pollution over the NCP area, or more precisely, increased the number of haze days. Associated physical mechanisms were further examined. Due to the high albedo and efficient reflections, the local SST in October became cooler than the climate mean state, showing the radiative cooling effect. The responses of the atmospheric circulations initially manifested as anomalous cyclonic circulation in the upper troposphere, and then developed into cyclonic and anti-cyclonic circulations on both sides of the Beaufort Sea in the subsequent November. The decreased surface wind through the Bering Strait could not transport cold seawater to the Bering Sea as usual and led to a warmer sea surface over the Bering Sea. The reduction of surface wind speed over the Gulf of Alaska weakened the seawater evaporation and the latent heat release, which conserved more thermal energy in the sea surface, i.e., positive SST anomalies.

The November SST anomalies over the Bering Sea and Gulf of Alaska acted as a bridge in the close relationship between the BSISO ($R=0.43$, exceeding the 99% confidence level) and HDJ_{NCP} ($R=0.61$). The warmer sea surface efficiently heated the air above and resulted in significant responses in the atmosphere. In the upper-troposphere, zonal west wind anomalies prevailed in the mid-high latitudes, and the meridionality of the atmosphere was reduced, indicating the decrease of the southward cold air activities. A “+–+” Rossby wave-like train propagated from North China and the Japan Sea, through the Bering Sea and Gulf of Alaska, to the Cordillera Mts. Near the surface, the NPO-like pattern and the negative SLP anomalies over Eurasia induced southerly anomalies over the coastal area of China, providing a calm and moist environment for haze formation. In addition, the intensity of the thermal inversion over the NCP area was significantly enhanced, and the clear, dry and cold air was difficult to transport to the surface. The horizontal and vertical dispersions were both limited, so the fine particles were apt to accumulate and cause haze pollution. The linkages and corresponding physical mechanisms were well reproduced via the large CESM-LE ensembles, confirming the causality.

In this study, the response of the number of haze days in early winter in the North China plain to the autumn Beaufort Sea ice and the associated physical mechanisms were investigated. As shown in Figure 2, the HDJ_{NCP} was 42.7 days and reached its maximum in 2015. Thus, the measurements in 2015 were composited after removing the linear trend to verify the results from the observational analyses (Figure 17). In September-October 2015, there were positive sea ice anomalies on the west of the Beaufort Sea (Figure 17a), which satisfied the close relationship revealed in this study. Meanwhile, an obviously warmer SST in November was observed in most of the BA region (Figure 17b), transferring the impacts of the BSISO. As a result, a weaker East Asia jet stream, an anomalous southerly (Figure 17c), limited horizontal and vertical dispersion

conditions, and moist air (Figure 17d) enhanced the early-winter haze pollution in 2015. However, some questions remain unanswered and should be investigated with numerical models in future work. For example, the internal dynamic and thermal processes and how the positive sea ice anomalies (radiative cooling) affected the atmospheric circulations, are not fully understood. During this work, linear correlation analyses were the main research technique, and the linear relationship was discovered. In fact, the dynamic–thermodynamic processes in the air-ice interaction are neither straightforward nor necessarily linear (Zhang et al., 2000; Gao et al., 2015). Considering the contradiction among the results by a single numerical model (Gao et al., 2015), a multi-model ensemble was required to solve the internal physical mechanisms. Furthermore, the November SST anomalies over the Bering Sea and Gulf of Alaska were treated as a bridge to connect the sea ice and the haze pollution. It is necessary to examine whether this bridge was constructed all the time. Particularly, after 2010, haze pollution became more serious. The driven role of the BSISO and the bridge of SST_{BA} needs to be verified. Moreover, as revealed by the EOF decomposition, the number of haze days in southern China varied differently. Its relationship with the sea ice in the Arctic is still unclear and needs to be addressed. The significant relationship revealed in this study and associated previous work potentially improved the monthly prediction of haze pollution. Valuable haze predictions are urgently needed by the scientific decision-making departments to control haze pollution in China (Wang, 2018).

Acknowledgements

This research was supported by the National Natural Science Foundation of China (41705058 and 91744311), the National Key Research and Development Plan (2016YFA0600703), the CAS–PKU Partnership Program, and the funding of the Jiangsu Innovation & Entrepreneurship team.

Reference

- Cai, W. J., Li, K., Liao, H., Wang, H. J., Wu, L. X.: Weather Conditions Conducive to Beijing Severe Haze More Frequent under Climate Change, *Nature Climate Change*, doi:10.1038/nclimate3249, 2017.
- Chen, H. P. and Wang, H. J.: Haze Days in North China and the associated atmospheric circulations based on daily visibility data from 1960 to 2012. *J. Geophys. Res.*, 120, 5895–5909, doi:10.1002/2015JD023225, 2015.
- Chen, H. P., Wang, H. J., Sun, J. Q., Xu, Y. Y., and Yin, Z. C.: Anthropogenic Fine Particulate Matter Pollution Will Be Exacerbated in Eastern China Due to 21st-Century GHG Warming, *Atmos. Chem. Phys. Discuss.*, <https://doi.org/10.5194/acp-2018-761>, in review, 2018.
- Cohen, J. L., Furtado, J. C., Barlow, M. A., Alexeev, V. A., Cherry, J. E.: Arctic warming, increasing snow cover and widespread boreal winter cooling, *Environ Res Lett*, 7,014007, 2012.

- Dee, D. P., Uppala, S. M., Simmons, A. J., Berrisford, P., Poli, P., Kobayashi, S., Andrae, U., Balmaseda, M. A., Balsamo, G., Bauer, P., Bechtold, P., Beljaars, A. C. M.: The ERA-Interim reanalysis: configuration and performance of the data assimilation system. *Q. J. Roy. Meteor. Soc.*, 137, 553–597, doi:10.1002/qj.828, 2011.
- 305 Deser, C., Tomas, R. A., Peng, S.: The transient atmospheric circulation response to north atlantic sst and sea ice anomalies, *Journal of Climate*, 20(18), 4751, 2007.
- Ding, Y. H., Liu, Y. J.: Analysis of long-term variations of fog and haze in China in recent 50 years and their relations with atmospheric humidity, *Sci. China Ser. D: Earth Sci*, 57, 36–46 (in Chinese), 2014.
- Fan, K., Xie, Z. M., Wang, H. J., Xu, Z. Q., Liu, J. P.: Frequency of spring dust weather in North China linked to sea ice variability in the Barents Sea, *Climate Dynamics*, doi: <https://doi.org/10.1007/s00382-016-3515-7>, 2017.
- 310 Gao, Y., Chen, D.: A dark October in Beijing 2016, *Atmos. Oceanic Sci. Lett.*, 10 (3), 206–213, 2017.
- Gao, Y. Q., Sun J. Q., Li F., et al.: Arctic Sea Ice and Eurasian Climate: A Review, *Adv. Atmos. Sci.*, 32(1), 92–114, 2015.
- He, C., Liu, R., Wang, X. M., Liu, S. C., Zhou, T. J., Liao W. H.: How does El Niño-Southern Oscillation modulate the interannual variability of winter haze days over eastern China? *Science of the Total Environment*, 651, 1892–1902, doi: <https://doi.org/10.1016/j.scitotenv.2018.10.100>, 2019.
- 315 He, S. P.: Asymmetry in the Arctic Oscillation Teleconnection with January Cold Extremes in Northeast China, *Atmos. Oceanic Sci. Lett.*, 8(6), 386–391, doi: 10.3878/AOSL20150053, 2015.
- Honda, M., Inoue, J., Yamane, S.: Influence of low Arctic sea ice minima on anomalously cold Eurasian winters, *Geophys. Res. Lett.*, 36, L08707, doi: 10.1029/2008GL037079, 2009.
- 320 Kalnay, E., Kanamitsu, M., Kistler, R., Collins, W., Deaven, D., Gandin, L., Iredell, M., Saha, S., White, G., Woollen, J., Zhu, Y., Leetmaa, A., Reynolds, R., Chelliah, M., Ebisuzaki, W., Higgins, W., Janowiak, J., Mo, K. C., Ropelewski, C., Wang, J., Jenne, R., Joseph, D.: The NCEP/NCAR 40-year reanalysis project, *Bull. Am. Meteorol. Soc.*, 77, 437–471, doi: 10.1175/1520-0477(1996)077<0437: TNYRP>2.0.CO; 2, 1996.
- Kay, J. E., and Coauthors: The Community Earth System Model (CESM) Large Ensemble Project: A community resource for studying climate change in the presence of internal climate variability. *Bull. Amer. Meteor. Soc.*, 96, 1333–1349, 2015.
- 325 Kim, B. M., Son, S. W., Min, S. K., Jeong, J. H., Kim, S. J., Zhang, X.D., Shim, T., Yoon, J. H.: Weakening of the stratospheric polar vortex by Arctic sea-ice loss, *Nature Communications*, doi: 10.1038/ncomms5646, 2014.
- Li, F., Wang, H. J.: Autumn Eurasian snow depth, autumn Arctic sea ice cover and East Asian winter monsoon, *Int. J. Climatol.*, doi: 10.1002/joc.3936 s, 2014.
- 330 Li, F., Wang, H. J.: Autumn sea ice cover, winter northern hemisphere annular mode, and winter precipitation in Eurasia, *J. Climate*, 26(11), 3968–3981, 2012.
- Li, F., Wang, H. J.: Relationship between Bering sea ice cover and East Asian winter monsoon Year-to-Year Variations, *Adv. Atmos. Sci.*, 30(1), 48–56, 2013.
- Li, F., Wang, H. J., Gao, Y. Q.: On the strengthened relationship between East Asian winter monsoon and Arctic Oscillation: A comparison of 1950–1970 and 1983–2012. *J. Climate*, 27, 5075–5091, doi: 10.1175/JCLI-D-13-00335.1. 2014.
- 335 Li, F., Wang, H. J., Gao, Y. Q.: Change in Sea Ice Cover is Responsible for Non-Uniform Variation in Winter Temperature over East Asia. *Atmos. Oceanic Sci. Lett.*, 8(6), 376–382, doi: 10.3878/AOSL20150039. 2015.
- Li, K., Liao, H., Cai, W., Yang, Y.: Attribution of anthropogenic influence on atmospheric patterns conducive to recent most severe haze over eastern China, *Geophys. Res. Lett.*, 45(4), 2072–2081, doi:10.1002/2017GL076570, 2018.

- 340 Li, S. L., Han, Z., Chen, H. P.: A Comparison of the Effects of Interannual Arctic Sea Ice Loss and ENSO on Winter Haze Days: Observational Analyses and AGCM Simulations, *J. Meteor. Res.*, 31(5), 820–833, doi: 10.1007/s13351-017-7017-2, 2017.
- Liu, J. P., Curry J. A., Wang, H. J., Song, M., Horton, R. M.: Impact of declining Arctic sea ice on winter snowfall, *Proc. Natl. Acad. Sci. U.S.A.*, 109, 4074–4079, 2012.
- 345 Liu, J. P., Zhang, Z. H., Horton, R. M., Wang, C. Y., Ren, X. B.: Variability of North Pacific Sea Ice and East Asia North Pacific Winter Climate, *J. Climate*, 20, 1991–2001, doi:10.1175/JCLI4105.1, 2007.
- Rayner, N. A., D. E. Parker, E. B. Horton, C. K. Folland, L. V. Alexander, D. P. Rowell, E. C. Kent, and A. Kaplan.: Global analyses of sea surface temperature, sea ice, and night marine air temperature since the late nineteenth century, *J. Geophys. Res.*, 108, 4407, doi:10.1029/2002JD002670, 2003.
- 350 Rogers, J. C.: The North Pacific Oscillation, *International Journal of Climatology*, 1(1), 39–57. doi:10.1002/joc.3370010106, 1981.
- Sun, X. C., Han Y. Q., Li, J., et al.: Analysis of the Influence of Vertical Movement on the Process of Fog and Haze with Air Pollution, *Plateau Meteorology* (in Chinese), 36(4), 1106–1114, 2017.
- Wang, H. J., Chen, H. P., Liu J. P.: Arctic sea ice decline intensified haze pollution in eastern China, *Atmos. Oceanic Sci. Lett.*, 8 (1): 1–9, 2015.
- 355 Wang, H. J., Chen, H. P.: Understanding the recent trend of haze pollution in eastern China: role of climate change, *Atmos. Chem. Phys.*, 16, 4205–4211, 2016.
- Wang, H. J.: On assessing haze attribution and control measures in China, *Atmospheric and Oceanic Science Letters*, 11, 2, 120–122, DOI: 10.1080/16742834.2018.1409067, 2018.
- 360 Wang, S. Y., Liu, J. P.: Delving into the relationship between autumn Arctic sea ice and central–eastern Eurasian winter climate, *Atmos. Oceanic Sci. Lett.*, 9(5), 366–374, doi: 10.1080/16742834.2016.1207482, 2016.
- Xu, X. P., Li, F., He, S. P., Wang, H. J.: Subseasonal reversal of East Asian surface temperature variability in winter 2014/15, *Adv. Atmos. Sci.*, 35(6), <https://doi.org/10.1007/s00376-017-7059-5>, 2018.
- 365 Yang, Y., Liao, H., Lou, S.: Increase in winter haze over eastern China in recent decades: Roles of variations in meteorological parameters and anthropogenic emissions, *J. Geophys. Res. Atmos.*, 121, 13050–13065, 2016.
- Yin, Z. C., Wang, H. J.: The relationship between the subtropical Western Pacific SST and haze over North-Central North China Plain, *International Journal of Climatology*, 36, 3479–3491, DOI: 10.1002/joc.4570, 2016a.
- Yin, Z. C., Wang, H. J.: Seasonal prediction of winter haze days in the north central North China Plain, *Atmos. Chem. Phys.*, 16, 14843–14852, <https://doi.org/10.5194/acp-16-14843-2016>, 2016b.
- 370 Yin, Z. C., Wang, H. J. Role of Atmospheric Circulations on Haze Pollution in December 2016, *Atmos. Chem. Phys.*, 17, 11673–11681, doi: 10.5194/acp-17-11673-2017, 2017a.
- Yin, Z. C., Wang, H. J.: Statistical Prediction of Winter Haze Days in the North China Plain Using the Generalized Additive Model, *Journal of Applied Meteorology and Climatology*, 56, 2411–2419, DOI: <https://doi.org/10.1175/JAMC-D-17-0013.1>, 2017b.
- 375 Yin, Z. C., Wang, H. J., Chen, H. P.: Understanding severe winter haze events in the North China Plain in 2014: roles of climate anomalies, *Atmos. Chem. Phys.*, 17, 1641–1651, doi:10.5194/acp-17-1641-2017, 2017.
- Yin, Z. C., Wang, H. J., Guo, W. L.: Climatic change features of fog and haze in winter over North China and Huang-Huai Area, *SCIENCE CHINA Earth Sciences*, 58(8), 1370–1376, 2015.

- 380 Yin, Z. C., Wang, H. J., Ma, X. H.: Possible Linkage between the Chukchi Sea Ice in the Early Winter and the February Haze
Pollution in the North China Plain, *Climate Dynamics*. under review, 2018.
- Zhang, J. T., Rothrock, D., Steele, M.: Recent changes in Arctic sea ice: The interplay between ice dynamics and
thermodynamics, *J. Climate*, 13, 3099–3314, 2000.
- Zhang, Q. Q., Ma, Q., Zhao, B., et al.: Winter haze over North China Plain from 2009 to 2016: Influence of emission and
meteorology, *Environmental Pollution*, 242, 1308–1318, 2018.
- 385 Zhou, W.: Impact of Arctic amplification on East Asian winter climate, *Atmos. Oceanic Sci. Lett.*, 10(5), 385–388, doi:
10.1080/16742834.2017.1350093, 2017.

390

395 **Table and Figures captions**

Table 1. The correlation coefficient (CC) between the BSISO (HDJ_{NCP}) and SST indices in October, November, and
December. The linear trend was removed. ‘*’ indicates that the CCs exceed the 95% confidence level, and ‘***’ indicates that
the CCs exceed the 99% confidence level. The meanings of the abbreviations were also explained.

400 **Figure 1.** The spatial pattern (shading) of the first EOF mode (variation contribution: 33%) for HDJ from 1979 to 2015. The
black crosses and dots represent the locations of the observation stations. The cross (dot) indicated that the HDJ accounted
for more (less) than 70% of the total winter haze days.

Figure 2. The variation of (a) HDJ_{NCP} from 1979 to 2015 and (b) daily maximum $PM_{2.5}$ from December to January in 2015
over the NCP area. The error bars in panel (a) represent one standard error among the measured sites.

405 **Figure 3.** The correlation coefficient (CC) between the HDJ_{NCP} and September-October sea ice concentration from 1979 to
2015, after detrending. The black dots indicate CCs exceeding the 95% confidence level (t test). The black box represents the
selected Beaufort Sea.

Figure 4. Distributions of the September-October sea ice concentration after removal of the linear trend in typical years (i.e.,
the year when $|BSISO| > 0.8 \times$ its standard deviation). The “+” and “-” represent the mathematical sign of the BSISO and
 HDJ_{NCP} indices. The “.sig” indicates that the absolute value of the index anomaly was larger than $0.8 \times$ its standard deviation.

410 **Figure 5.** The CC between the BSISO and SST in (a) October, (b) November, and (c) December, from 1979 to 2015, after
detrending. The black dots indicate CCs exceeding the 95% confidence level (t test). The black boxes (WB: west of Beaufort
Sea, BS: Bering Sea and GA: Gulf of Alaska) are the significantly correlated areas, which were used to calculate the SST
indices.

Figure 6. The CC between BSISO and September-October (a) geopotential height (shading), wind (arrow) at 500 hPa, (c)

415 SLP (shade), and surface wind (arrow); and November (b) geopotential height (shading), wind (arrow) at 500 hPa, (d) SLP
(shade), and surface wind (arrow) from 1979 to 2015, after detrending. The white dots indicate CCs exceeding the 90%
confidence level (t test). The black box in (a–d) represents the location of the Beaufort Sea.

Figure 7. The distribution of the climate mean surface wind (arrow) in November and the CC between the BSISO and
surface wind speed in November from 1979 to 2015, after detrending. The black dots indicate CCs exceeding the 95%
420 confidence level (t test). The black boxes (RS1 and RS2) are the significantly correlated areas, which were used to calculate
the $WSPD_{RS1}$ and $WSPD_{RS2}$ index.

Figure 8. The CC between $WSPD_{RS2}$ and SST in November from 1979 to 2015. The black dots indicate that the CCs
exceeded the 95% confidence level (t test). The black box represents the BA area. The linear trend was removed.

Figure 9. The CC between $WSPD_{RS1}$ and (a) SST and (b) latent heat flux in November from 1979 to 2015. The black dots
425 indicate that the CCs exceeded the 95% confidence level (t test). The black box represents the BA area. The linear trend was
removed.

Figure 10. The variation of the normalized BSISO (blue) and November SST_{BA} (green) from 1979 to 2015, after detrending.

Figure 11. The CC between November SST_{BA} and (a) omega at 200 hPa, (b) at 1000 hPa in December and January from
1979 to 2015. The black dots indicate that the CCs exceeded the 95% confidence level (t test). The linear trend was removed.
430 The black box represents the BA area.

Figure 12. The CC between the November SST_{BA} and (a) zonal wind at 200 hPa, (b) wind (arrow), geopotential height
(shading) at 500 hPa, (c) wind (arrow), geopotential height (shading) at 850 hPa, (d) surface wind (arrow), and SLP (shading)
in December-January from 1979 to 2015. The black dots indicate that the CCs exceeded the 95% confidence level (t test).
435 The linear trend was removed. The black boxes in panel (b) represent the three anomalous centers at 500 hPa, and the gray
and black boxes in panel (d) represent the negative and positive anomalous centers.

Figure 13. The variation of the November normalized SST_{BA} (gray, bar) and area-averaged geopotential height at 500 hPa of
the three anomalous centers (west: black, middle: green, east: orange) from 1979 to 2015, after detrending.

Figure 14. The CC between the November SST_{BA} and (a) surface wind (arrow), specific humidity (shading) at 1000 hPa (b)
BLH (shading), thermal inversion potential (contour, solid (dashed) green lines indicate that the positive (negative)
440 correlations exceeded the 90% confidence level (t test)) from 1979 to 2015. The black dots indicate that the CCs exceeded
the 90% confidence level (t test). The linear trend was removed. The black boxes represent the NCP area. The thermal
inversion potential was defined as the air temperature at 850 hPa minus SAT.

Figure 15. The cross-section (114°E–120°E mean) CC between (a) the HDJ_{NCP} , (b) November SST_{BA} and omega (shading),
wind (arrow) in December-January from 1979 to 2015. The black dots indicate that the CCs exceeded the 95% confidence
445 level (t test). The linear trend was removed.

Figure 16. Composite difference of (a) September-October sea ice concentration, (b) sea surface temperature in November,
(c) geopotential height (contour) at 500 hPa, surface specific humidity in December-January, (d) BLH (shading), surface
wind (arrow) in December-January. The black box in panel (a) represents the location of the Beaufort Sea, and in panel (b) it
represents the BA area. Results are based on 35 ensembles of CESM-LE simulations. The black dots indicate that
450 mathematical sign of the changes with shading from more than 50% of the members are consistent with the ensemble mean.

Figure 17. The distributions of (a) September-October sea ice concentration in 2015, (b) sea surface temperature in
November 2015, (c) geopotential height (shading) at 500 hPa, wind (arrow) at 200 hPa in December-January 2015, (d)
specific humidity (shading) at 1000 hPa, BLH (black dots indicate that its value is negative), $WSPD$ (contour, solid black
lines indicate a negative value) in December-January 2015. The black box in panel (a) represents the location of the Beaufort
455 Sea, and in panel (b) it represents the BA area. The linear trend was removed.

Table 1. The correlation coefficient (CC) between the BSISO (HDJ_{NCP}) and SST indices in October, November, and December. The linear trend was removed. ‘*’ indicates that the CCs exceed the 95% confidence level, and ‘***’ indicates that the CCs exceed the 99% confidence level. The meanings of the abbreviations were also explained.

CC		Oct	Nov	Dec
BSISO: Beaufort Sea Ice in Sep-Oct	SST_{WB}: SST over the west of the Beaufort Sea	-0.75**	-0.26	-0.23
	SST_{BS}: SST over the Bering Sea	0.27	0.41*	0.45**
	SST_{GA}: SST over the Gulf of Alaska	0.31	0.40*	0.44**
	SST_{BA}: SST _{BS} + SST _{GA}	0.34*	0.43**	0.48**
HDJ_{NCP}: Haze days in Dec-Jan	SST_{WB}: SST over the west of the Beaufort Sea	-0.30	-0.05	-0.10
	SST_{BA}: SST _{BS} + SST _{GA}	0.52**	0.61**	0.56**

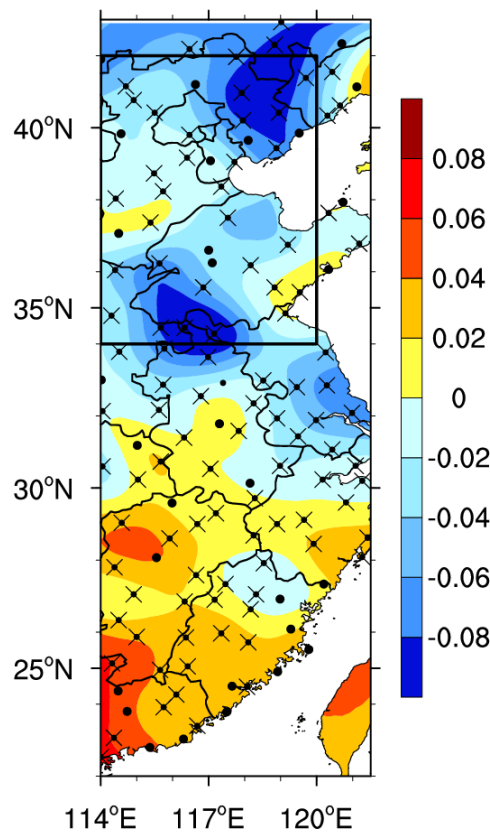


Figure 1. The spatial pattern (shading) of the first EOF mode (variation contribution: 33%) for HDJ from 1979 to 2015. The black crosses and dots represent the locations of the observation stations. The cross (dot) indicated that the HDJ accounted for more (less) than 70% of the total winter haze days.

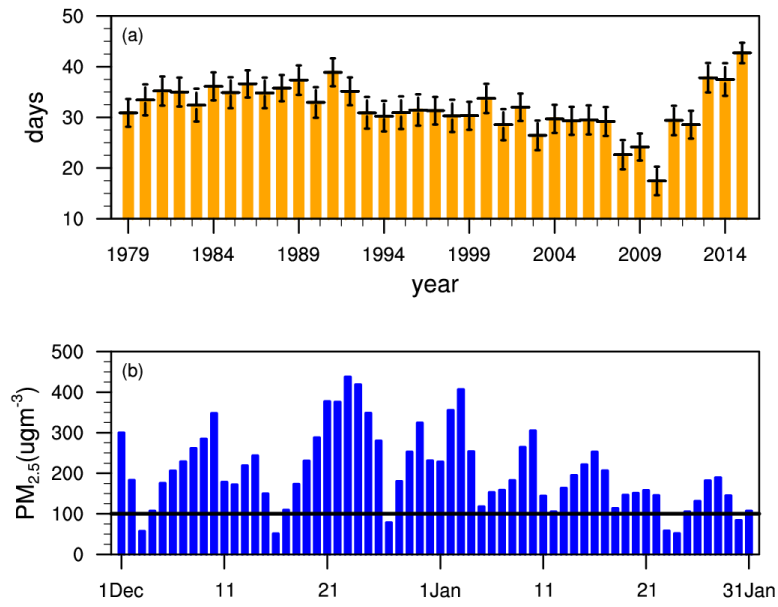


Figure 2. The variation of (a) HDJ_{NCP} from 1979 to 2015 and (b) daily maximum PM_{2.5} from December to January in 2015 over the NCP area. The error bars in panel (a) represent one standard error among the measured sites.

470

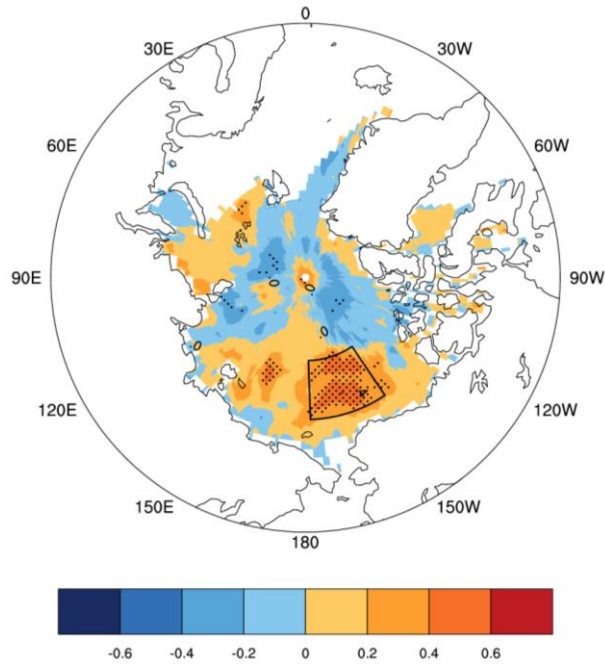
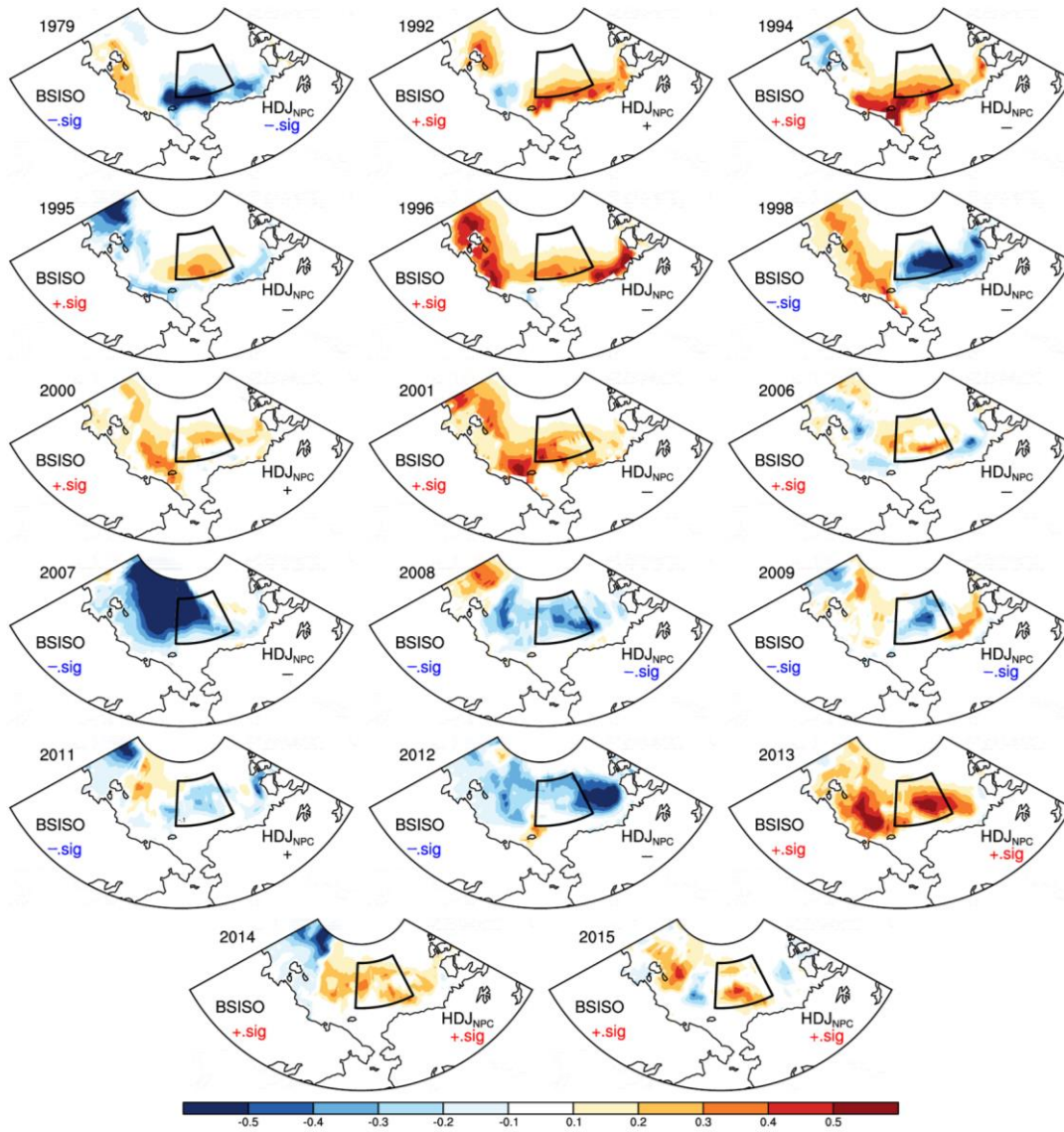
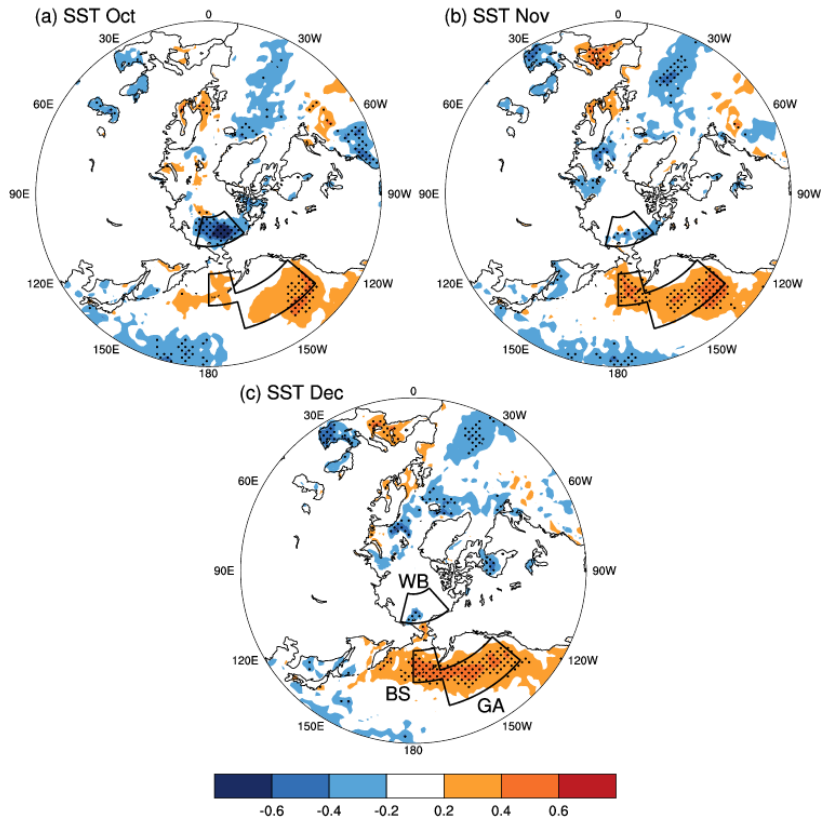


Figure 3. The correlation coefficient (CC) between the HDJ_{NCP} and September-October sea ice concentration from 1979 to 2015, after detrending. The black dots indicate CCs exceeding the 95% confidence level (t test). The black box represents the selected Beaufort Sea.

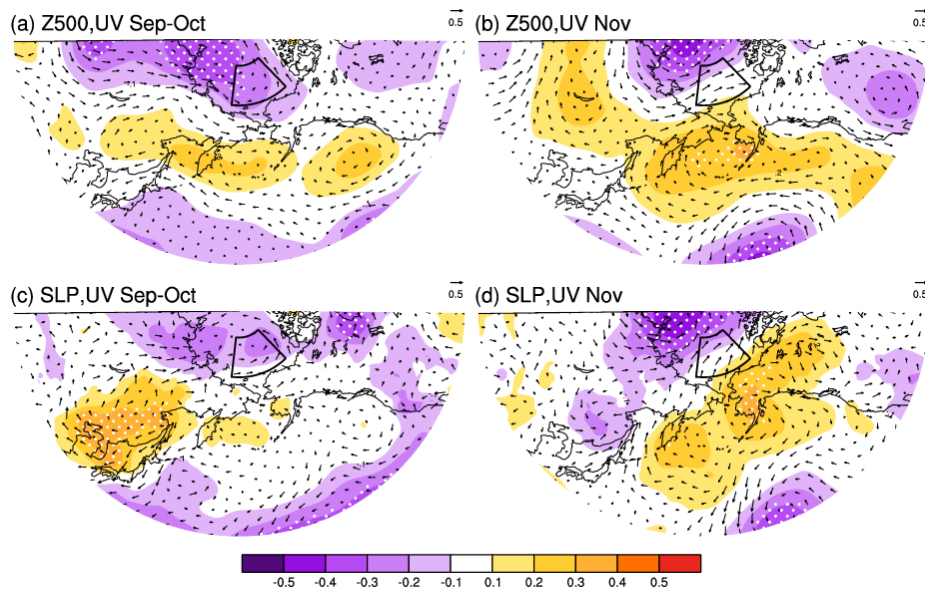


475

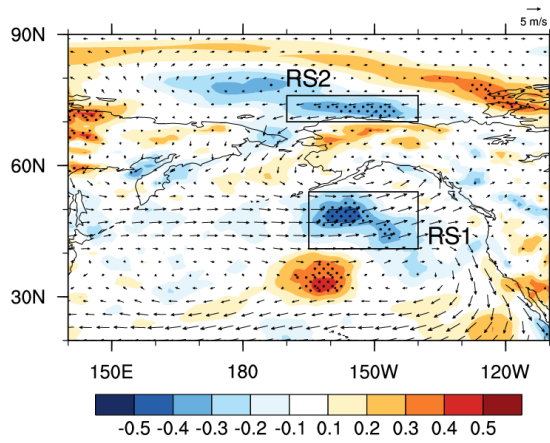
Figure 4. Distributions of the September-October sea ice concentration after removal of the linear trend in typical years (i.e., the year when $|\text{BSISO}| > 0.8 \times \text{its standard deviation}$). The “+” and “-” represent the mathematical sign of the BSISO and HDJ_{NPC} indices. The “.sig” indicates that the absolute value of the index anomaly was larger than $0.8 \times \text{its standard deviation}$.



480 **Figure 5.** The CC between the BSISO and SST in (a) October, (b) November, and (c) December, from 1979 to 2015, after detrending. The black dots indicate CCs exceeding the 95% confidence level (t test). The black boxes (WB: west of Beaufort Sea, BS: Bering Sea and GA: Gulf of Alaska) are the significantly correlated areas, which were used to calculate the SST indices.



485 **Figure 6.** The CC between BSISO and September-October (a) geopotential height (shading), wind (arrow) at 500 hPa, (c) SLP (shade), and surface wind (arrow); and November (b) geopotential height (shading), wind (arrow) at 500 hPa, (d) SLP (shade), and surface wind (arrow) from 1979 to 2015, after detrending. The white dots indicate CCs exceeding the 90% confidence level (t test). The black box in (a–d) represents the location of the Beaufort Sea.



490 **Figure 7.** The distribution of the climate mean surface wind (arrow) in November and the CC between the BSISO and surface wind speed in November from 1979 to 2015, after detrending. The black dots indicate CCs exceeding the 95% confidence level (t test). The black boxes (RS1 and RS2) are the significantly correlated areas, which were used to calculate the $WSPD_{RS1}$ and $WSPD_{RS2}$ index.

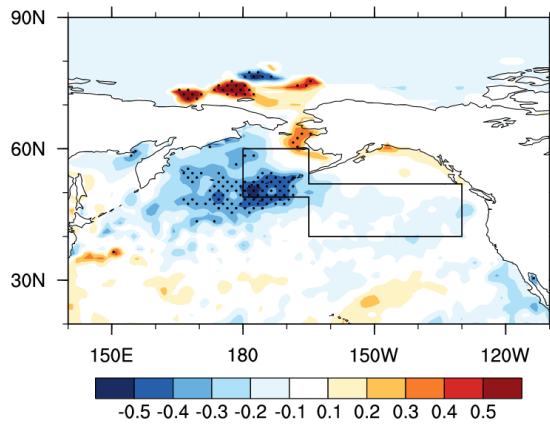
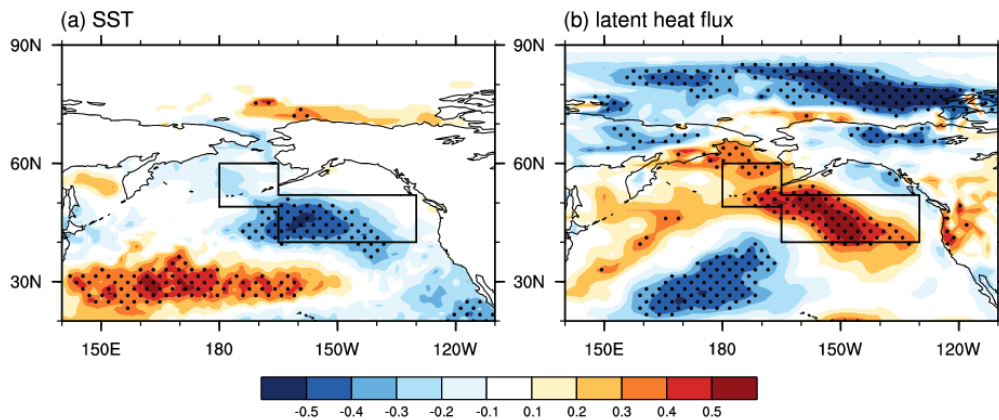


Figure 8. The CC between $WSPD_{RS2}$ and SST in November from 1979 to 2015. The black dots indicate that the CCs exceeded the 95% confidence level (t test). The black box represents the BA area. The linear trend was removed.



495 **Figure 9.** The CC between $WSPD_{RS1}$ and (a) SST and (b) latent heat flux in November from 1979 to 2015. The black dots indicate that the CCs exceeded the 95% confidence level (t test). The black box represents the BA area. The linear trend was removed.

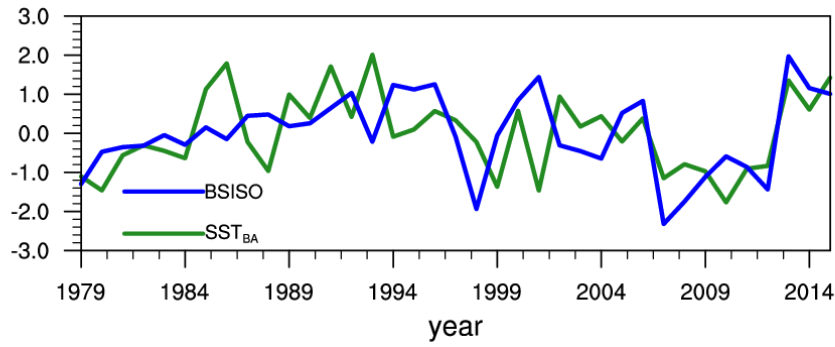
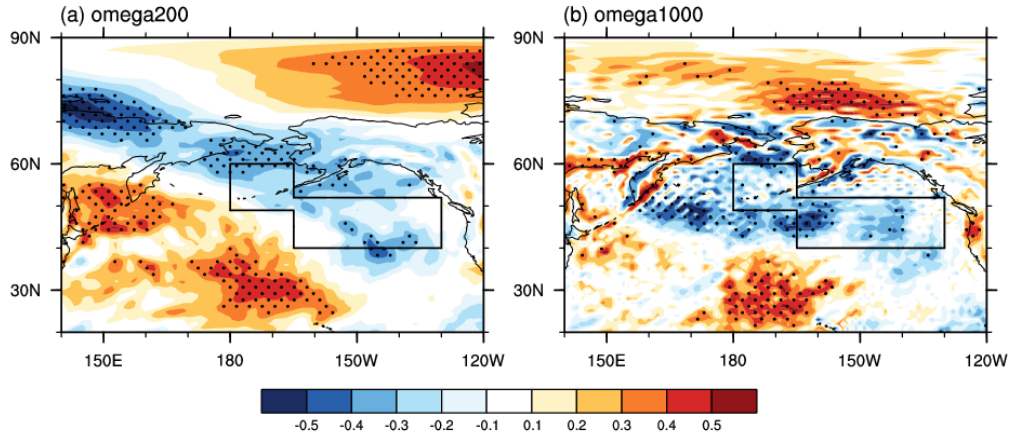
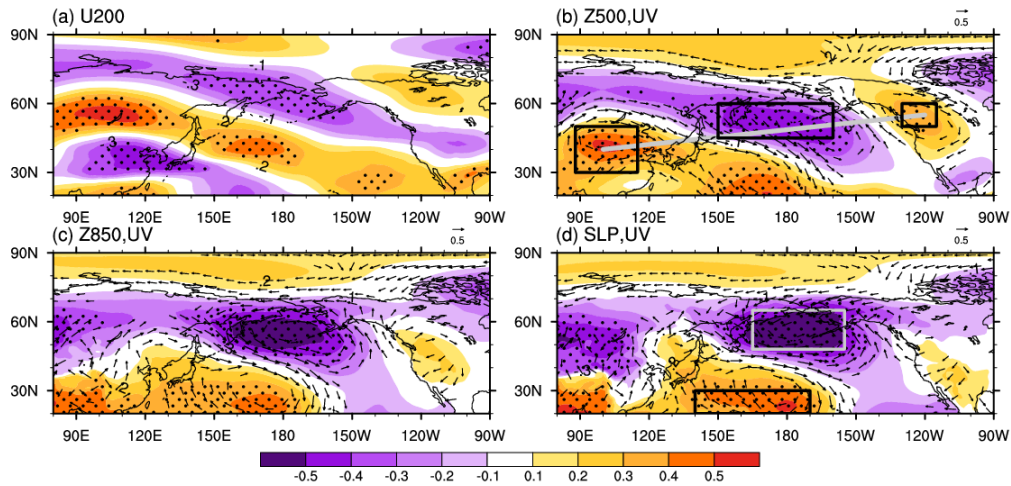


Figure 10. The variation of the normalized BSISO (blue) and November SST_{BA} (green) from 1979 to 2015, after detrending.



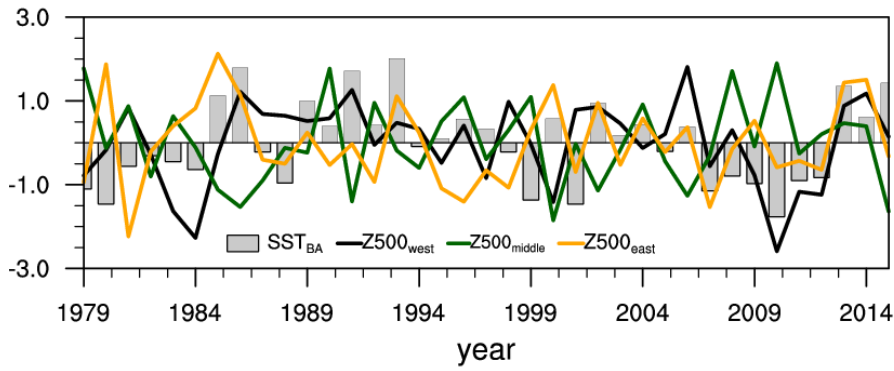
500

Figure 11. The CC between November SST_{BA} and (a) omega at 200 hPa, (b) at 1000 hPa in December and January from 1979 to 2015. The black dots indicate that the CCs exceeded the 95% confidence level (t test). The linear trend was removed. The black box represents the BA area.



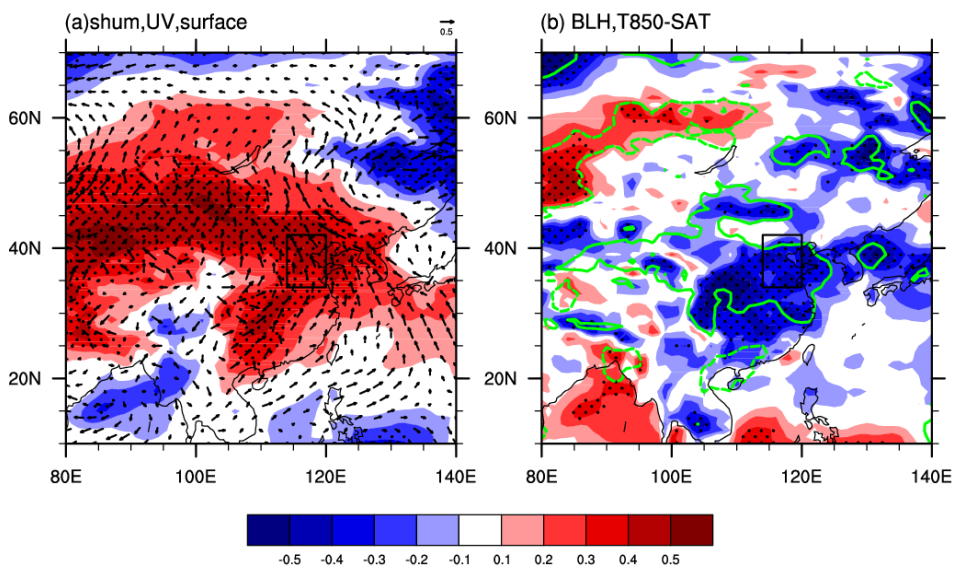
505

Figure 12. The CC between the November SST_{BA} and (a) zonal wind at 200 hPa, (b) wind (arrow), geopotential height (shading) at 500 hPa, (c) wind (arrow), geopotential height (shading) at 850 hPa, (d) surface wind (arrow), and SLP (shading) in December-January from 1979 to 2015. The black dots indicate that the CCs exceeded the 95% confidence level (t test). The linear trend was removed. The black boxes in panel (b) represent the three anomalous centers at 500 hPa, and the gray and black boxes in panel (d) represent the negative and positive anomalous centers.



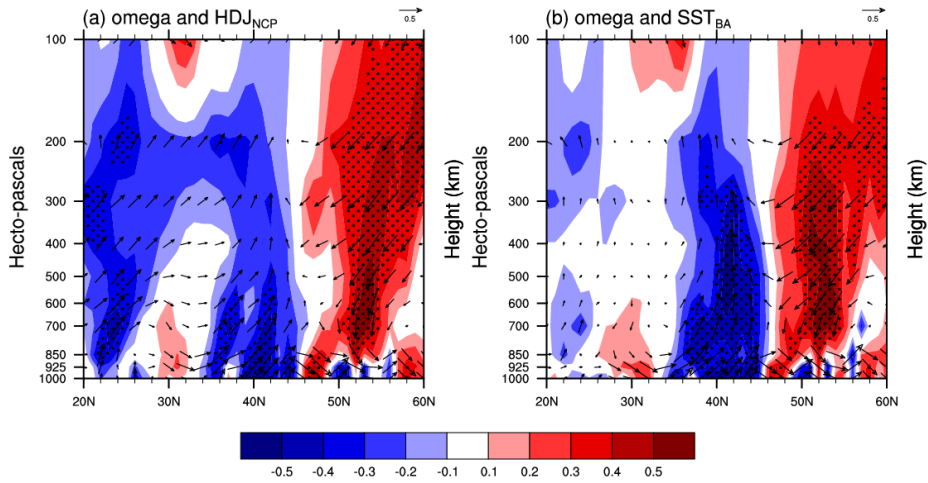
510

Figure 13. The variation of the November normalized SST_{BA} (gray, bar) and area-averaged geopotential height at 500 hPa of the three anomalous centers (west: black, middle: green, east: orange) from 1979 to 2015, after detrending.

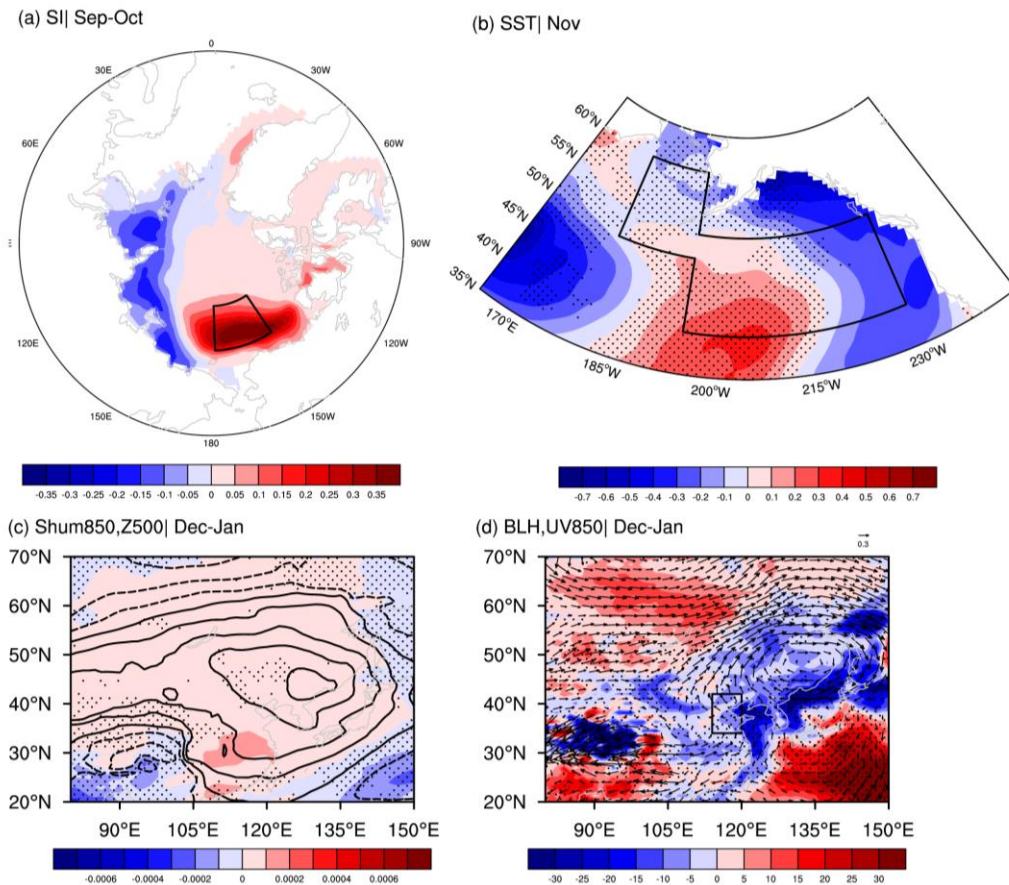


515

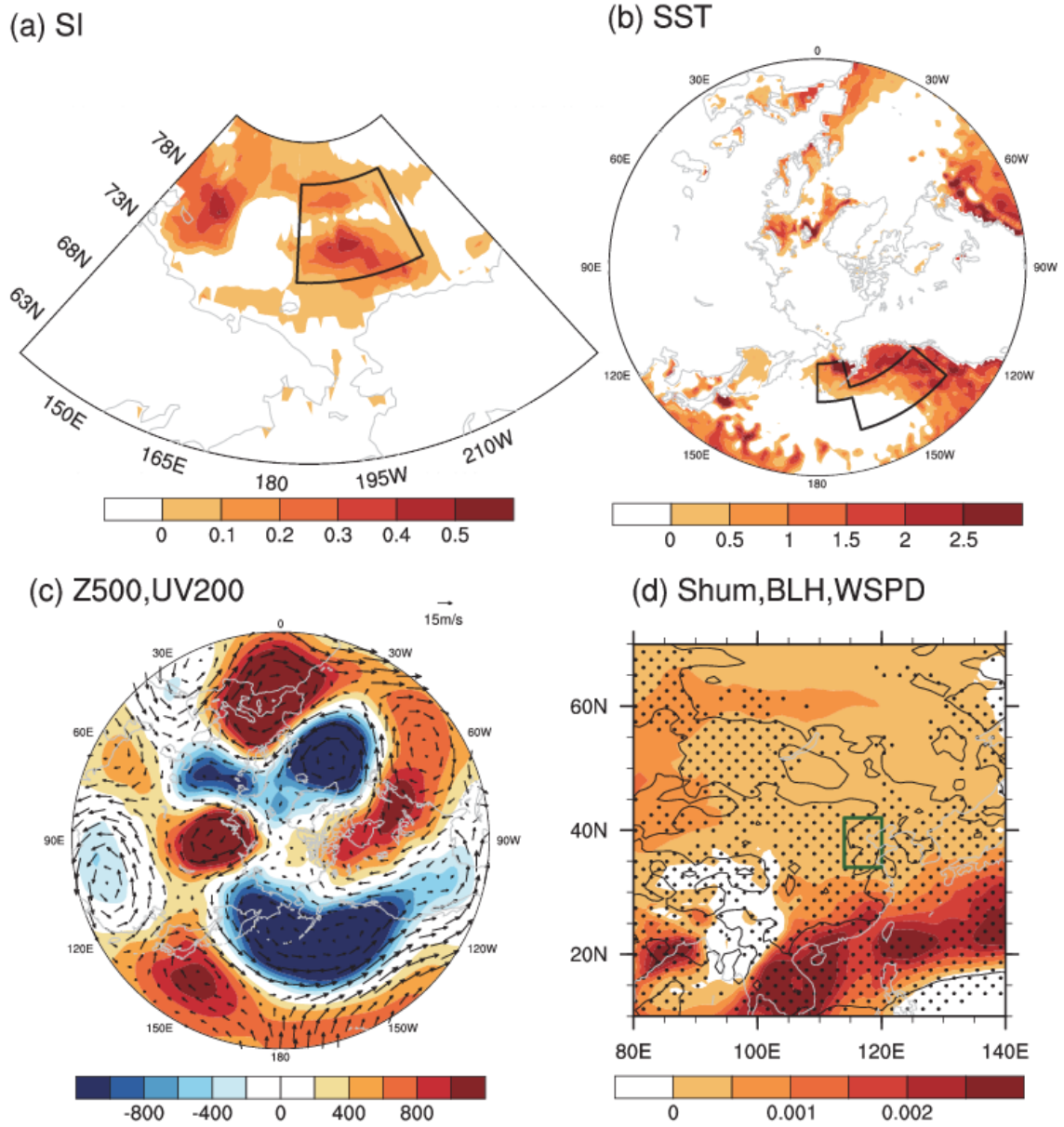
Figure 14. The CC between the November SST_{BA} and (a) surface wind (arrow), specific humidity (shading) at 1000 hPa (b) BLH (shading), thermal inversion potential (contour, solid (dashed) green lines indicate that the positive (negative) correlations exceeded the 90% confidence level (t test)) from 1979 to 2015. The black dots indicate that the CCs exceeded the 90% confidence level (t test). The linear trend was removed. The black boxes represent the NCP area. The thermal inversion potential was defined as the air temperature at 850 hPa minus SAT.



520 **Figure 15.** The cross-section (114 E–120 E mean) CC between (a) the HDJ_{NCP}, (b) November SST_{BA} and omega (shading), wind (arrow) in December-January from 1979 to 2015. The black dots indicate that the CCs exceeded the 95% confidence level (t test). The linear trend was removed.



525 **Figure 16.** Composite difference of (a) September-October sea ice concentration, (b) sea surface temperature in November, (c) geopotential height (contour) at 500 hPa, specific humidity at 850 hPa in December-January, (d) BLH (shading), wind (arrow) at 850 hPa in December-January. The black box in panel (a) represents the location of the Beaufort Sea, and in panel (b) it represents the BA area. Results are based on 35 ensembles of CESM-LE simulations. The black dots indicate that mathematical sign of the changes with shading from more than 50% of the members are consistent with the ensemble mean.



530 **Figure 17.** The distributions of (a) September-October sea ice concentration in 2015, (b) sea surface temperature in November 2015, (c) geopotential height (shading) at 500 hPa, wind (arrow) at 200 hPa in December-January 2015, (d) specific humidity (shading) at 1000 hPa, BLH (black dots indicate that its value is negative), WSPD (contour, solid black lines indicate a negative value) in December-January 2015. The black box in panel (a) represents the location of the Beaufort Sea, and in panel (b) it represents the BA area. The linear trend was removed.